CAR-TR-700 DACA76-92-C-0009
CS-TR-3218 February 1994

An Improved Shape from Shading Algorithm

Hemant Singh

Department of Electrical Engineering
University of Maryland
College Park, MD 20742-3285

Rama Chellappa

Department of Electrical Engineering
Center for Automation Research, and
Institute for Advanced Computer Studies
University of Maryland
College Park, MD 20742-3275

Abstract

We propose an improved shape from shading (SFS) algorithm which is an extension of the recently published algorithm by Zheng and Chellappa [13]. A markedly more accurate estimate of the azimuth of the illumination source is presented. Depth reconstruction has been improved upon by using a new set of boundary conditions and adapting a more sophisticated technique for hierarchical implementation of the SFS algorithm. Errors at the boundaries of images and in rotation of the reconstructed images have been corrected. Typical results on synthetic and real images are presented.

The support of the Advanced Research Projects Agency (ARPA Order No. 8459) and the U.S. Army Topographic Engineering Center under Contract DACA76-92-C-0009 is gratefully acknowledged, as is the help of Sandy German in preparing this paper.

1 Introduction

We present an improved version of the SFS algorithm suggested recently by Zheng and Chellappa [13]. A significantly improved azimuth angle estimator of the illuminant is demonstrated. Some of the reconstruction errors obtained by the authors of [13] have been eliminated by adopting a more sophisticated hierarchical implementation of the SFS algorithm. Essentially our algorithm is the same as that in [13] but by changing boundary conditions and preserving the reflectance map between resolution layers during reconstruction we have been able to remove warping and rotation errors in image reconstructions. The notation used in this report is similar to that used in [13].

To estimate the illuminant direction from the images we first need a model relating image intensity to illuminant source. In computer vision research, one of the most commonly used image formation models is the Lambertian model [6, 7, 8]. Assuming orthographic projection with the z axis parallel to the optical axis of the camera and the positive z direction pointing toward the camera, the Lambertian model can be written as

$$\begin{aligned} \mathcal{R}(p,q) &= \eta \cos\theta_i + \sigma_0 \\ &= \eta(\vec{N}.\vec{L}) + \sigma_0 \\ &= \eta(\cos(\alpha-\tau)\sin\beta\sin\tau + \cos\beta\cos\gamma) + \sigma_0 \end{aligned} \tag{1}$$

where η is the composite albedo, which includes factors such as strength of the illumination and reflectivity of the surface. θ_i, the incidence angle, is the angle between the surface normal and the direction toward the light source. $\vec{L} = (\cos\tau\sin\gamma, \sin\tau\sin\gamma, \cos\gamma)$ is the unit vector in the illuminant direction where τ, called the azimuth of the illuminant, is the angle between $\vec{L}$ and the x-z plane. γ, the slant angle, is the angle between $\vec{L}$ and the positive z axis ($\frac{\pi}{2} - \gamma$ is the elevation of the illuminant). $\vec{N} = (N_x, N_y, N_z) = (\cos\alpha\sin\beta, \sin\alpha\sin\beta, \cos\beta)$ is the surface normal at position $(x, y, z(x,y))$, where $\alpha = \alpha(x,y)$ and $\beta = \beta(x,y)$ are the azimuth and slant angles of the surface normal at $(x, y, z(x,y))$. σ_0 is the bias brightness, which depends on background illumination, digitizer calibration, and so on.

Under the assumptions of a Lambertian surface, point light source, and uniform albedo, the reflectance map is determined by the parameters τ, γ, η, and σ_0.

The organization of this report is as follows: Section 2 presents the improved estimation of the azimuth angle of illuminant. We have used a different set of boundary conditions for the edge and corner pixels of an image for this azimuth estimation. A good improvement over the azimuth estimates of [13] has been achieved for the same images used in [13].

Section 3 presents the changes that we incorporated into the SFS algorithm and its modified implementation. The SFS algorithm essentially remains the same except that now the reflectance map is preserved in transition across the pyramidal layers. Also the boundary conditions have been changed while reconstructing the height map.

In Section 4, we present typical examples illustrating the improved results obtained. We first show some simple geometric shaded objects and SFS results on these. A cylinder and hyperbola are used because some doubts were expressed in [13] about the implementation of SFS on such objects. Then we show how warping and rotation errors in reconstruction of the Mozart image can be removed using our modified algorithm. Results for some other multiple-object and occluded images are also shown. Conclusions are given in Section 5.

2 Improved Estimation of Azimuth Angle of Illuminant

The image model that has been used is that of Section II(A) of [13]. We have concentrated on the local voting method [13] because it has given more consistent results than the other contour-based method [13] for a variety of images. For completeness we shall first describe the local voting estimator and then describe the changes made to the estimation technique that have led to significantly improved estimation.

We start with the assumption that for any image point $(x_0, y_0, z(x_0, y_0))$, its neighbors can be approximated by a spherical patch [13] with $(a(x_0, y_0), b(x_0, y_0), c(x_0, y_0))$ being the center of the sphere, and $r(x_0, y_0)$ the radius of the sphere (here the sphere is a local approximation; the radius and center of the sphere depend on the local surface shape); α and β are the tilt and slant angles of the surface normal.

For a small increment along the direction $\vec{s} = (\delta x, \delta y)$, the corresponding increment in (α, β) is $(\delta\alpha_s, \delta\beta_s)$ and the following relations hold:

$$\delta x = -r \sin\beta \sin\alpha \delta\alpha_s + r \cos\beta \cos\alpha \delta\beta_s \tag{2}$$

$$\begin{aligned} \delta y &= -r\sin\beta\cos\alpha\delta\alpha_s + r\cos\beta\sin\alpha\delta\beta_s \quad (3) \\ \sin\beta\delta\beta_s &= -\frac{\frac{x-a}{r}\cdot\frac{\delta x}{r} - \frac{y-b}{r}\cdot\frac{\delta y}{r}}{\sqrt{1-\left(\frac{x-a}{r}\right)^2-\left(\frac{y-b}{r}\right)^2}} \\ &= \frac{\sin\beta\cos\alpha\delta x - \sin\beta\sin\alpha\delta y}{r\cos\beta} \quad (4) \end{aligned}$$

On the other hand, from the image model (1), an increment in intensity due to $(\delta\alpha_s, \delta\beta_s)$ is

$$\delta I_s = \eta[-\sin(\alpha-\tau)\sin\beta\sin\gamma\delta\alpha_s + \cos(\alpha-\tau)\cos\beta\sin\gamma\delta\beta_s - \sin\beta\cos\gamma\delta\beta_s]. \quad (5)$$

Substitution of (3–5) into (6) leads to

$$\begin{aligned} \delta I_s &= \eta[(\cos\alpha\sin\beta\sin\gamma\delta\alpha_s + \sin\alpha\cos\beta\sin\gamma\delta\beta_s)\sin\tau + \\ &\quad (-\sin\alpha\sin\beta\sin\gamma\delta\alpha_s + \cos\alpha\cos\beta\sin\gamma\delta\beta_s)\cos\tau - \\ &\quad \frac{\sin\beta\cos\alpha\delta x + \sin\beta\sin\alpha\delta y}{r\cos\beta}\cos\gamma] \\ &= \frac{\eta}{r}(\delta x, \delta y)\begin{bmatrix} \sin\gamma\cos\tau - \cos\gamma\tan\beta\cos\alpha \\ \sin\gamma\sin\tau - \cos\gamma\tan\beta\sin\alpha \end{bmatrix} \end{aligned}$$

Let $\vec{s}$ take different directions yielding

$$d\vec{I} = B\vec{X}$$

where

$$d\vec{I} = \begin{bmatrix} \delta I_1 \\ \delta I_2 \\ \vdots \\ \delta I_N \end{bmatrix}, \qquad B = \begin{bmatrix} \delta x_1 & \delta y_1 \\ \delta x_2 & \delta y_2 \\ \vdots & \vdots \\ \delta x_4 & \delta y_4 \end{bmatrix},$$

$$\vec{X} = \begin{bmatrix} \tilde{x}_L \\ \tilde{y}_L \end{bmatrix} = \frac{\eta}{r}\begin{bmatrix} \sin\gamma\cos\tau - \cos\gamma\tan\beta\cos\alpha \\ \sin\gamma\sin\tau - \cos\gamma\tan\beta\sin\alpha \end{bmatrix},$$

N is the number of measured directions for $\vec{s}$, and $\tilde{x}_L$ and $\tilde{y}_L$ are the x and y components of the local estimate of the azimuth of the illuminant. $\vec{X}$ can be solved using

$$\vec{X} = (B^tB)^{-1}B^td\vec{I}.$$

We have chosen B for eight directions (i.e. $N = 8$) around any pixel position in the image in such a way that B is given by

$$B = \begin{pmatrix} 1 & \frac{\sqrt{2}}{2} & 0 & -\frac{\sqrt{2}}{2} & -1 & -\frac{\sqrt{2}}{2} & 0 & \frac{\sqrt{2}}{2} \\ 0 & \frac{\sqrt{2}}{2} & 1 & \frac{\sqrt{2}}{2} & 0 & -\frac{\sqrt{2}}{2} & -1 & -\frac{\sqrt{2}}{2} \end{pmatrix}^t$$

The new boundary conditions that we have used for computing B are explained in Figure 1. For any pixel (marked by an X) on the boundary its eight neighbors (marked by circles) for computing B are shown in Figure 1. For the four corner pixels the eight neighboring pixels are also shown in Figure 1. Therefore the equations for the eight pixels to be used are given as

$$I(i,j) = I(i,j) - 2[I(i+1,j) - I(i,j+1) - I(i+1,j+1)] - I(i+2,j) - I(i,j+2) \quad (6)$$

It is shown in [13] that

$$\mathbf{E}_{x,y}\left\{\frac{\tilde{x}_L}{\tilde{x}_L^2 + \tilde{x}_L^2}\right\} = \cos\tau.F(\gamma) \quad (7)$$

and

$$\mathbf{E}_{x,y}\left\{\frac{\tilde{y}_L}{\tilde{x}_L^2 + \tilde{x}_L^2}\right\} = \sin\tau.F(\gamma) \quad (8)$$

where

$$F(\gamma) = \int_{\Omega_\beta} p(\beta)d\beta \frac{1}{2\pi}\int_{-\pi}^{\pi} \frac{\sin\gamma\cos\beta - \cos\gamma\sin\beta\cos\alpha}{\sqrt{\sin^2\gamma\cos^2\beta + \cos^2\gamma\sin^2\beta - \frac{1}{2}\sin 2\gamma\sin 2\beta\cos\alpha}} d\alpha. \quad (9)$$

$$\tau = \arctan\left(\frac{\mathbf{E}_{x,y}\{\frac{\tilde{y}_L}{\tilde{x}_L^2+\tilde{x}_L^2}\}}{\mathbf{E}_{x,y}\{\frac{\tilde{x}_L}{\tilde{x}_L^2+\tilde{x}_L^2}\}}\right). \quad (10)$$

We have chosen such boundary conditions because the boundary pixels are more likely to be correlated along the boundary rather than inside the image. The same logic is applied to the corner pixels where the weights are higher for boundary pixels rather than for inside pixels. By incorporating such a change in the azimuth estimator in [13] we obtained very good estimates of the azimuth. For the Mozart image the τ obtained in [13] for a ground truth of $\tau = 45$ degrees was 31.03 degrees whereas our estimate is 44.67823 degrees. We

have successfully tested this estimation scheme on a number of images and also on a number of azimuth angles of the Mozart image.

It should be pointed out that when doing local estimation, points where $d\vec{I} = \vec{0}$ have been ignored. Physically, these points correspond to a planar patch, where no estimation of the azimuth of the illuminant can be made based on local intensity information. Theoretically, errors are expected in this method due to the local spherical approximation. An extreme example is the case of a cylindrical surface, which cannot be approximated by spherical patches. For a cylindrical surface, the gradient of the image intensity, and hence the estimated azimuth of the illuminant, is always toward the direction perpendicular to the axis of the cylinder. However, as the local estimates on symmetric parts of a cylinder will cancel each other, the net error caused by a cylindrical patch is usually negligible [13]. This was a doubt expressed by Zheng and Chellappa [13] which we have verified by our algorithm to hold true. It will be shown in the next section that the local estimates do indeed cancel out and the algorithm is robust to reconstruction of a cylinder.

3 Modified SFS Algorithm

The formulation of the algorithm remains the same as that in Section III(A) of [13]. We have modified the hierarchical implementation of the algorithm as described below. In the implementation, the image resolution is reduced by a factor of 2 between adjacent resolution layers. The image size for the lowest resolution layer is 32. Let the variables with a tilde ($\tilde{}$) stand for the shape descriptors of the higher resolution layer while the variables without a tilde denote those of the lower resolution layer. The transition rules are the same as in [13].

For the implementation of the algorithm the more sophisticated pyramidal approach due to Peleg and Ron [14] has been used. A brief description of the technique is made here. For each image pixel the tangent of the elevation angle of the source, defined as T in [14], is computed as

$$T = \sqrt{p^2 + q^2} = \tan(\alpha_{\vec{N_s}}) \tag{11}$$

Given T, R [14] is computed from the image intensities as

$$R = \sqrt{\frac{1}{1+T^2}} \tag{12}$$

Based on the value T as computed in (12), the suggested algorithm for building the gray level pyramid for SFS purposes is as follows [14]:

1. T_0 is calculated from the given input image I_0 using (12).

2. A Gaussian pyramid $T_0, \ldots, T_{n-1}$ is built, whose base is T_0. The pyramid has N levels, chosen such that T_{n-1} will have significant shape information.

3. Using (12) the gray level image R_i is calculated for every pyramid level T_i. The images R_i constitute a gray level pyramid, which is the estimate of the reduced resolution surface reflectance.

4. The multi-resolution SFS algorithm is performed using the R_i pyramid. First, (p_{n-1}, q_{n-1}) are computed from R_{n-1} using the SFS algorithm. The obtained low resolution derivatives (p_i, q_i) are then expanded into (p_{i-1}, q_{i-1}) to be used as initial guesses for the computation of the (p, q) derivatives at level $i-1$ of the pyramid. The process is repeated until the (p, q) derivatives are computed for full resolution images.

4 Experimental Results

4.1 Azimuth Angle Estimates

To illustrate the utility of our illuminant direction and albedo estimators, we first tested the algorithm on a number of synthetic images. The tested images include 1) ellipses with ratio of major axis (parallel to the x axis) to minor axis equal to 2, 2) hyperbolas, 3) cylinders, and 4) a Mannequin image. For each case (except the Mannequin), the test images were generated using $\eta = 200$, σ_0 and various combinations of τ and γ. Figure 2 shows typical test images synthesized using $\tau = 45°$, $\gamma = 45°$, $\eta = 200$, and $\sigma_0 = 0$.

Figures 3, 4, and 5 show the estimates of the azimuth angle for the hyperbola, cylinder, and Mannequin images respectively. The plots in these three figures are presented in the

following order: (a) Estimation of τ for images generated with $\gamma = 45°$, $\eta = 200$, $\sigma_0 = 0$, and $\tau = 0°, 15°, 30°, \ldots, 345°$. (b) Estimation of τ for images generated with $\tau = 45$, $\eta = 200$, $\sigma_0 = 0$, and $\gamma = 0°, 15°, 30°, \ldots, 345°$.

As evident from these three figures the azimuth angle has been estimated to a high degree of accuracy for all the test images. It is a significant improvement over the corresponding results in [13]. The results for azimuth angle estimation for all images are summarized in Table 1.

Table 1: Azimuth Angle Estimates for Various Images

Image	τ	γ	τ(estimated)
Sphere	48°	90°	44.64°
Ellipse	48°	90°	44.64°
Ellipse	48°	90°	44.64°
Parabola	48°	90°	44.64°
Hyperbola	48°	90°	44.64°
Cylinder	48°	90°	44.64°
Sphere	48°	45°	44.64°
Ellipse	48°	45°	44.64°
Ellipse	48°	45°	44.64°
Parabola	48°	45°	44.64°
Hyperbola	48°	45°	44.64°
Cylinder	48°	45°	44.64°
Mozart	45°	45°	44.68°
Mozart	30°	45°	29.46°
Mozart	15°	45°	13.78°
Mannequin	45°	45°	44.58°
Mannequin	30°	45°	28.47°
Mannequin	15°	45°	13.74°

4.2 SFS Experiments

We tested our SFS algorithm on a number of images. In all the experiments we let $\mu = 1$ and $N_{\max}$ for the highest resolution layer be 500. The iterations start from $(p, q, Z) = (0, 0, 0)$ and the partial derivatives of the reflectance map, $\mathcal{R}_p$ and $\mathcal{R}_q$, are computed numerically. All the images presented in our examples are 256×256. The 3-D plots of height maps are reduced to 64×64 for clarity of presentation.

Figure 8 shows the comparison of the SFS results obtained here and in [13] (see Figure 5(j)–(l) of [13]) on the Mozart image. Warping errors are evident in the reconstructions of [13], especially in Figure 5(j) which is the reconstructed q map. Their q map and ours are shown in Figure 8(a) and (b) respectively. It is clear that by preserving the reflectance map and modifying boundary conditions we have been able to remove warping errors in reconstruction. More evidence of this for other real images is in the following paragraphs. Also note that the curls in the hair of Mozart are more pronounced in our map.

Figure 9 shows the SFS results on the synthetic Mannequin image. Figure 9(a) is the input image whose parameters have been estimated to be $\tau = 44.68°$, $\gamma = 45°$, $\eta = 250$, and $\sigma_0 = 0$. Figure 9(b) shows the image reconstructed by the SFS algorithm. A 3-D plot of (b) is shown in Figure 9(c). Figures 9(d) and (e) compare the p map of the ground truth and that obtained by SFS. Figures 9(f) and (g) compare the q map of the the ground truth and that obtained by SFS. A comparison of the reconstructed (Z, p, q) with the ground truth shows that the errors in the background region and a rotation distortion present in results of [13] (refer to Figures 5(e,h,j,l,n) of [13]) have been removed. We attribute this to the preserving of the reflectance map between resolution layers and the change in boundary conditions.

Figure 10(a) shows the input Lenna-2 image. The reflectance map parameters estimated by our algorithm are $\tau = 7.74°$, $\gamma = 59.52°$, $\eta = 192.01$, and $\sigma_0 = 3$. Figure 10(b) is the height map obtained by the SFS algorithm. Figure 10(c) shows the image reconstructed from the estimated parameters. Figure 10(d) shows a 3-D mesh plot of the height map obtained by SFS. Figure 10(e) and (f) show the p and q maps obtained from SFS. Figures 10(g)–(i) show images synthesized from the reconstructed (p, q) maps using the parameters $\gamma = 59.52°$, $\eta = 192.01$, and $\sigma_0 = 3$ and τ equal to $97.74°$, $187.74°$, $277.76°$ respectively, corresponding to illumination from the direction opposite or orthogonal to the estimated direction for the input image. It can be seen from Figures 10(b)–(e) that the shapes of the face and shoulder are recovered correctly and that features such as nose, lips, cheeks, chin, etc., are easily identified. The images synthesized from the SFS result using different illuminant directions are consistent.

Figure 11 shows another SFS experiment performed on multiply-occluded pepper images. Figure 11(a) shows the original image and Figure 11(b) shows the contour of the original

image. Figure 11(c) shows the height map obtained from SFS. The SFS estimated parameters were $\tau = 20.82°$, $\gamma = 58.02°$, $\eta = 225.78$, and $\sigma_0 = 0$. The image reconstructed by the SFS algorithm is shown in Figure 11(d) and its corresponding contour in Figure 11(e). For clarity the 3-D mesh plot (Figure 11(f)) of the reconstructed image is shown on a blow-up. As seen the contour maps are very similar and the mesh plot follows the contour of the multiple peppers quite well. An extensive comparison of 200 contour levels in each map was performed to determine whether the original and the reconstruction matched. They differ only in two levels; hence we conclude that the reconstruction of the height is accurate.

5 Conclusion

A more reliable and robust shape from shading algorithm based on the SFS algorithm given by Zheng and Chellappa has been presented. Boundary conditions have been modified in their algorithm and a more sophisticated hierarchical implementation of the algorithm has been implemented. As a result very good estimates of the azimuth angle of the illuminant have been obtained for a number of test images. Reconstruction errors around the boundary and rotational errors have been removed. A number of reconstructions have been performed for various images to verify the removal of these errors in reconstruction.

Acknowledgement

One of the authors (H.S.) is thankful to Deepak Kataria and Nanda Kumar of the Department of Computer Science, University of Maryland, for their help in the generation of synthetic shaded images and many helpful discussions. The Mannequin image was provided by Dr. Leclerc of the Artificial Intelligence Center, SRI.

Figure 2: Typical synthetic images used in estimating illuminant direction. The images shown are synthesized using the Lambertian reflectance map model with parameters $\tau = 45°$, $\gamma = 45°$, $\eta = 200$, and $\sigma_0 = 0$.

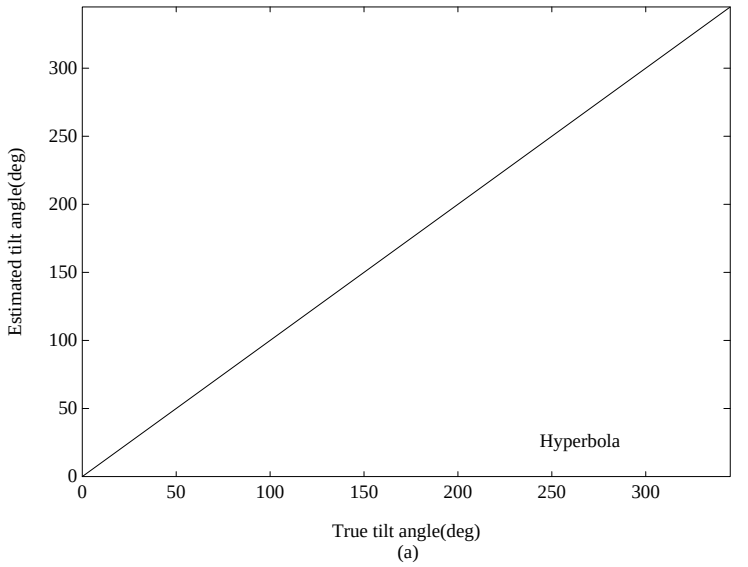

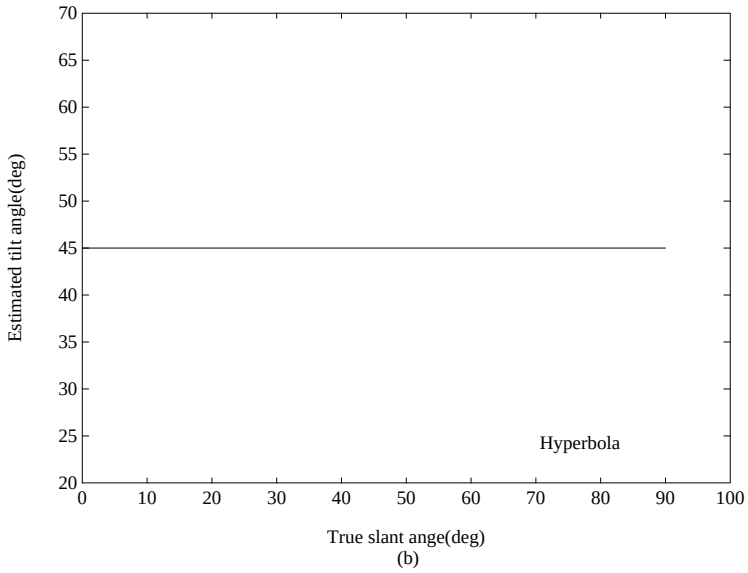

Figure 3: Estimation of azimuth angle for images of a hyperbola. (a) Estimation of τ for images generated with $\gamma = 45°$, $\eta = 200$, $\sigma_0 = 0$, and $\tau = 0,\ 15°,\ 30°, \ldots,\ 345°$. (b) Estimation of τ for images generated with $\tau = 45°$, $\eta = 200$, $\sigma_0 = 0$, and $\gamma = 0,\ 15°,\ 30°, \ldots,\ 90°$.

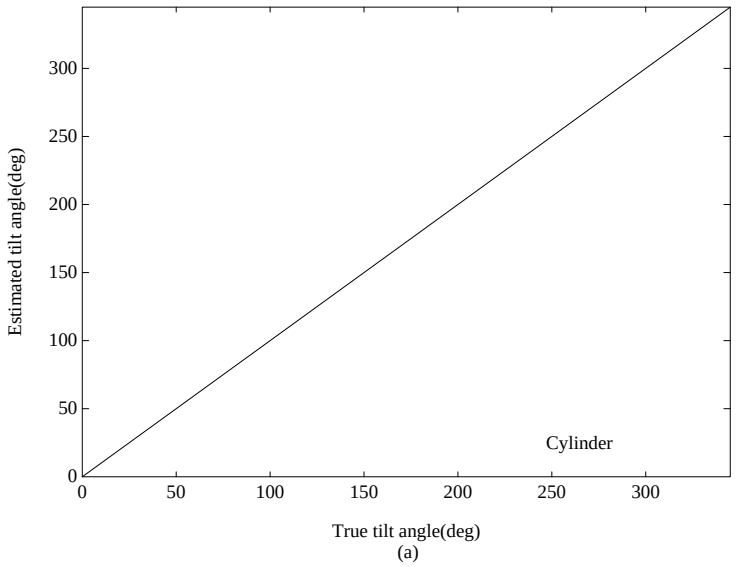

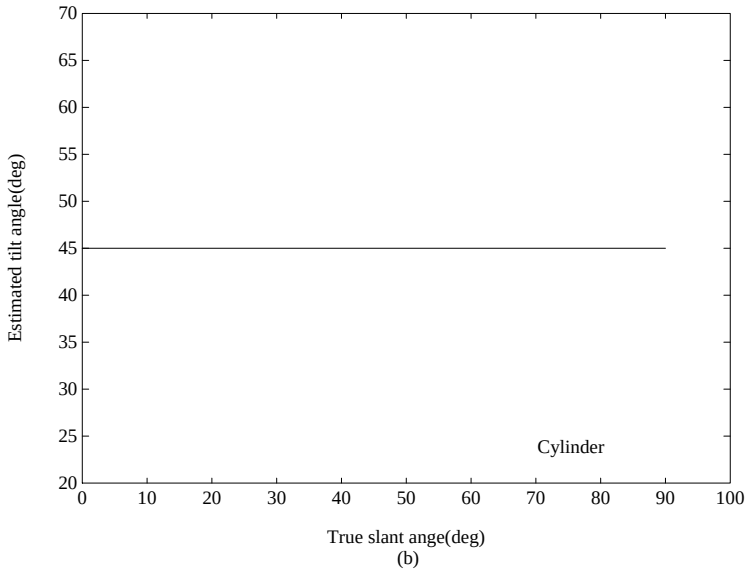

Figure 4: Estimation of azimuth angle for images of a cylinder. (a) Estimation of τ for images generated with $\gamma = 45°$, $\eta = 200$, $\sigma_0 = 0$, and $\tau = 0,\ 15°,\ 30°, \ldots, 345°$. (b) Estimation of τ for images generated with $\tau = 45°$, $\eta = 200$, $\sigma_0 = 0$, and $\gamma = 0,\ 15°,\ 30°, \ldots, 90°$.

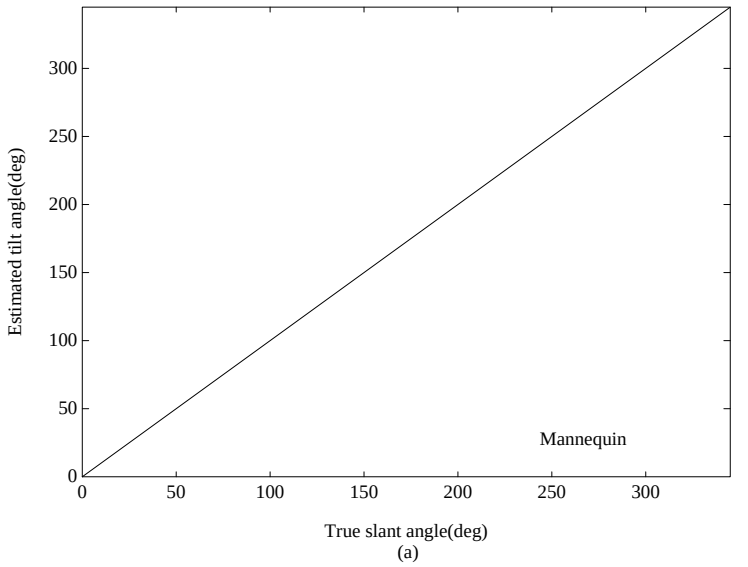

(a)

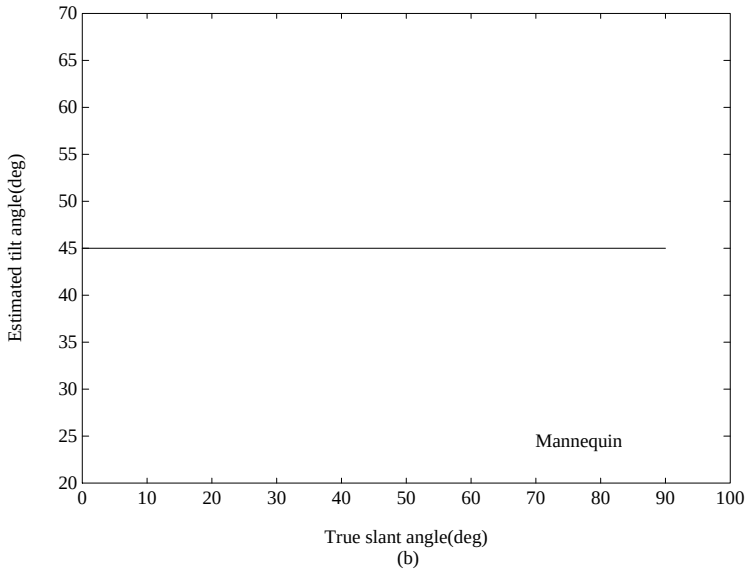

(b)

Figure 5: Estimation of azimuth angle for the Mannequin image. (a) Estimation of τ for images generated with $\gamma = 45°$, $\eta = 200$, $\sigma_0 = 0$, and $\tau = 0, 15°, 30°, \ldots, 345°$. (b) Estimation of τ for images generated with $\tau = 45°$, $\eta = 200$, $\sigma_0 = 0$, and $\gamma = 0, 15°, 30°, \ldots, 90°$.

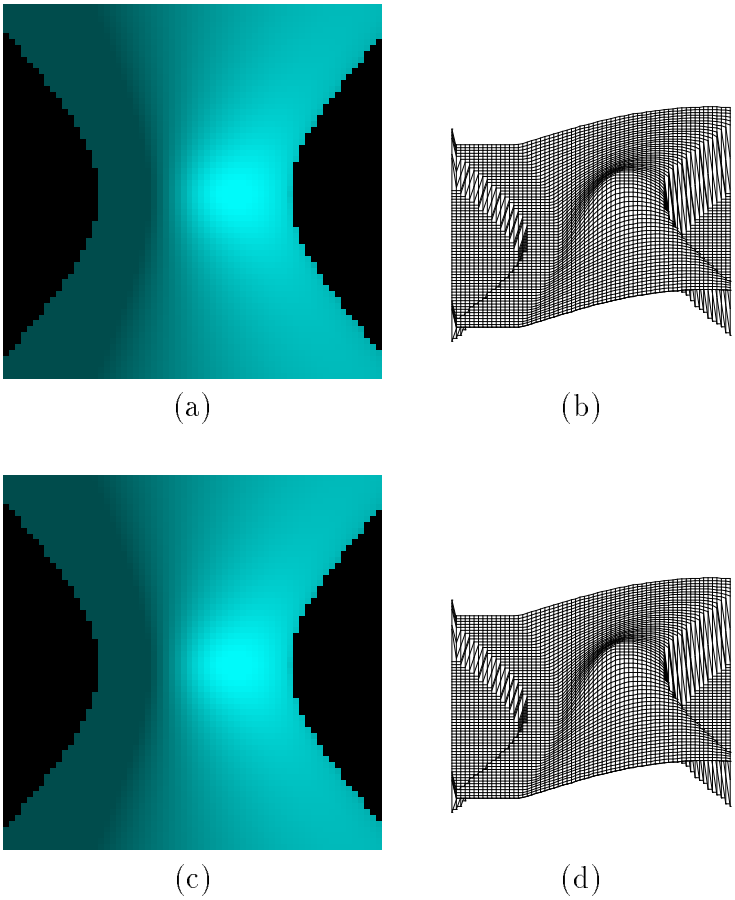

Figure 6: SFS experiment on the hyperbola image. (a) The input image. (b) True height map of image in (a). (c) The image synthesized with the SFS result. (d) SFS reconstructed height map.

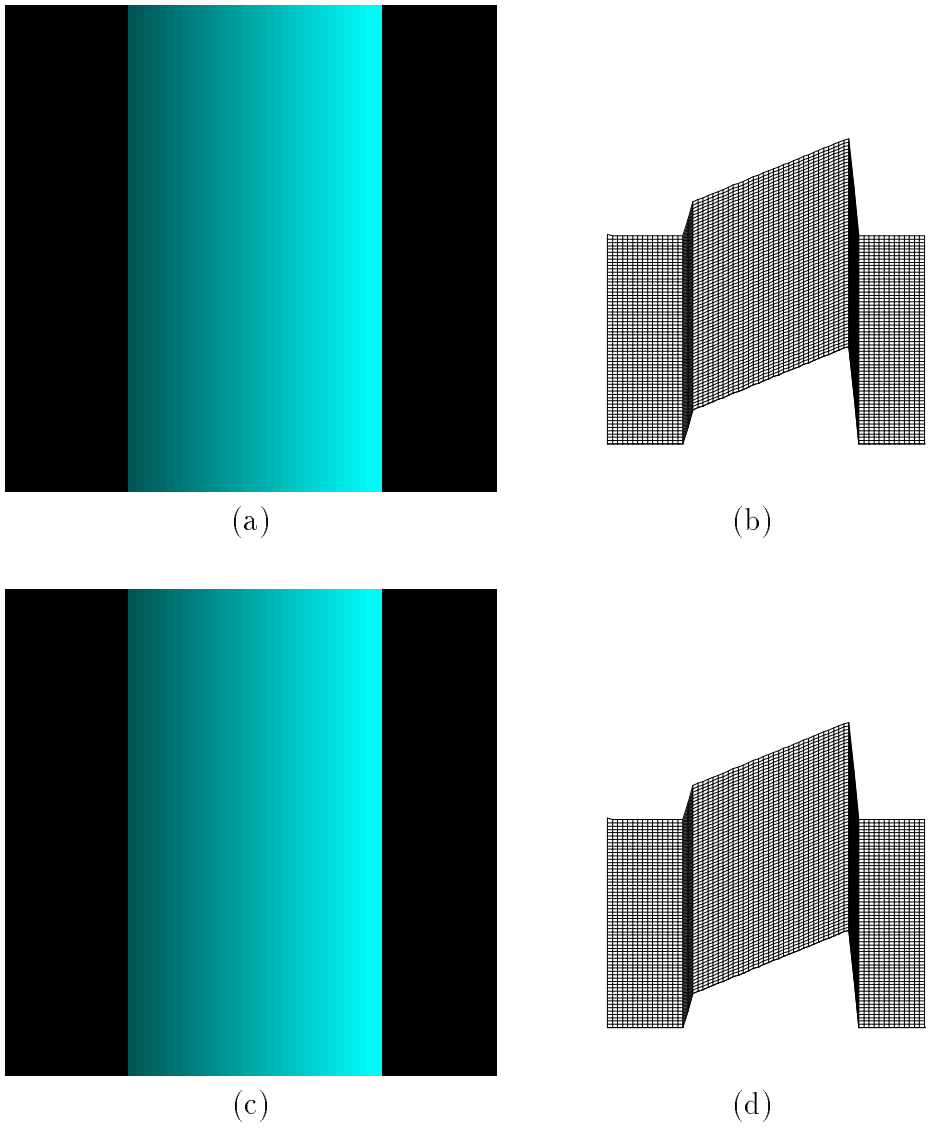

(a) (b)

(c) (d)

Figure 7: SFS experiment on the cylinder image. (a) The input image. (b) True height map of image in (a). (c) The image synthesized with the SFS result. (d) SFS reconstructed height map.

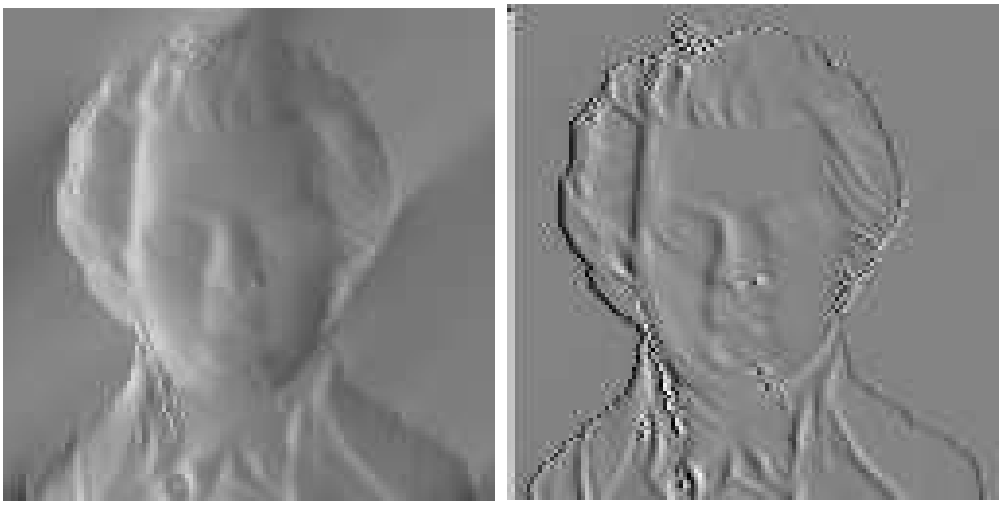

(a) (b)

Figure 8: Comparison of our results on the Mozart image to that of Zheng and Chellappa [13]. (a) The SFS reconstructed q map by Zheng and Chellappa [13]. (b) The SFS reconstructed q obtained by us.

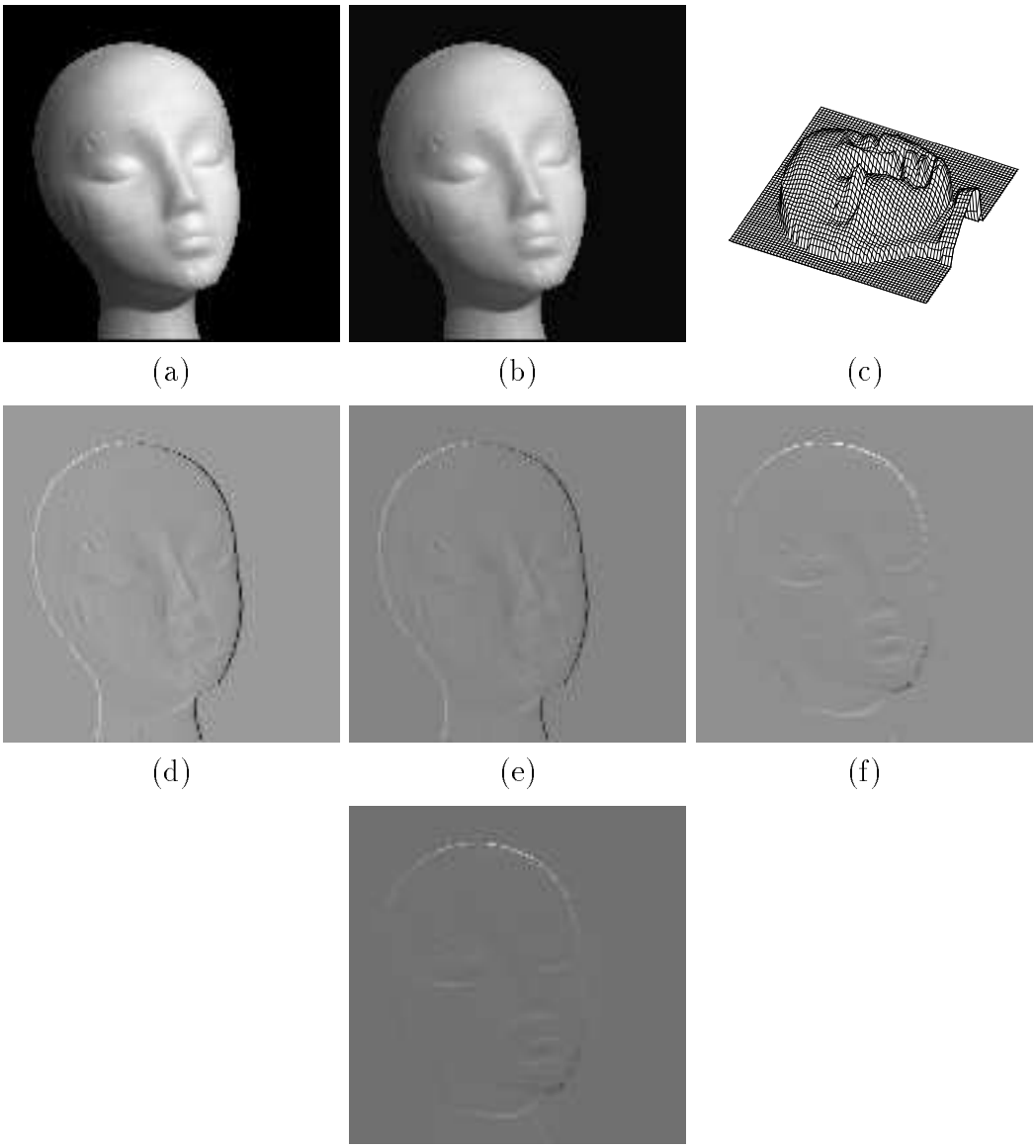

Figure 9: SFS experiment on the Mannequin image. (a) The input image. (b) The image generated from the SFS result using the estimated reflectance map parameters as the input image. (c) A 3-D plot of the reconstructed height map. (d) True Z_x map. (e) The SFS reconstructed p map. (f) True Z_y map. (g) The SFS reconstructed q map.

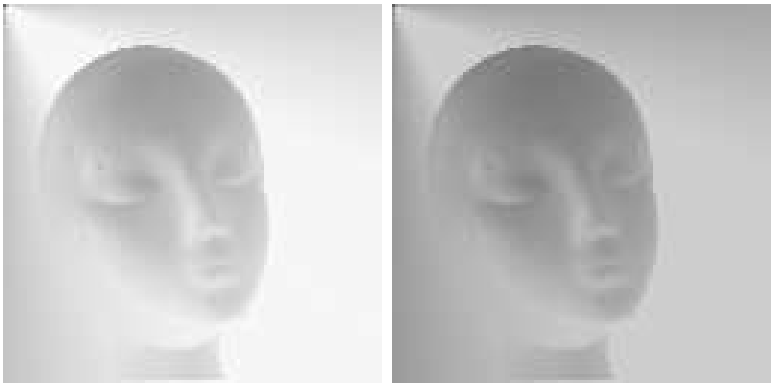

(h) (i)

(j) (k)

Figure 9: SFS experiment on the Mannequin image (contd.) (h) The image synthesized from the true height with $\tau = 135°$. (i) The image synthesized from the SFS result with $\tau = 135°$. (j) The image synthesized from the true height with $\tau = 225°$. (k) The image synthesized from the SFS result with with $\tau = 225°$.

(a) (b) (c)

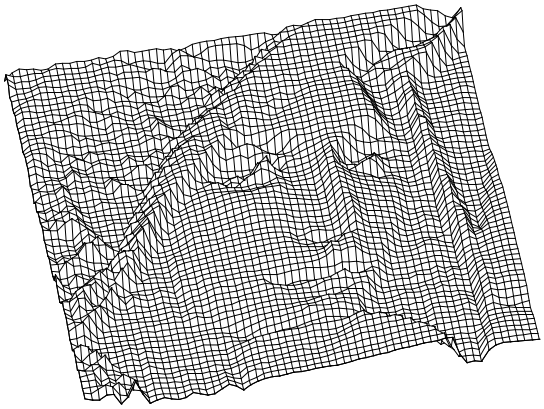

(d)

Figure 10: SFS experiment on the Lenna-2 image. (a) The input image. (b) The height map Z obtained by the SFS algorithm. (c) The image synthesized from the reconstructed height map with estimated parameters. (d) 3-D mesh plot of the height map obtained through SFS.

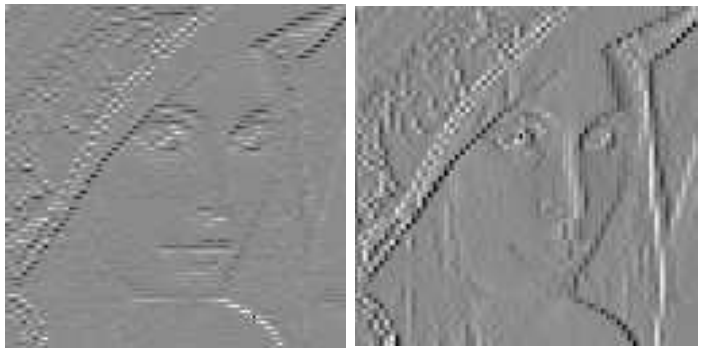

(e) (f)

(g) (h)

(i)

Figure 10: SFS experiment on Lenna-2 image (contd.). (e) The SFS reconstructed p map. (f) The SFS reconstructed q map. (g), (h) and (i) are images synthesized from the reconstructed (p, q) maps using τ equal to $97.74°$, $187.74°$, and $277.26°$, respectively, corresponding to illumination from the directions opposite or orthogonal to the estimated direction for the input image.

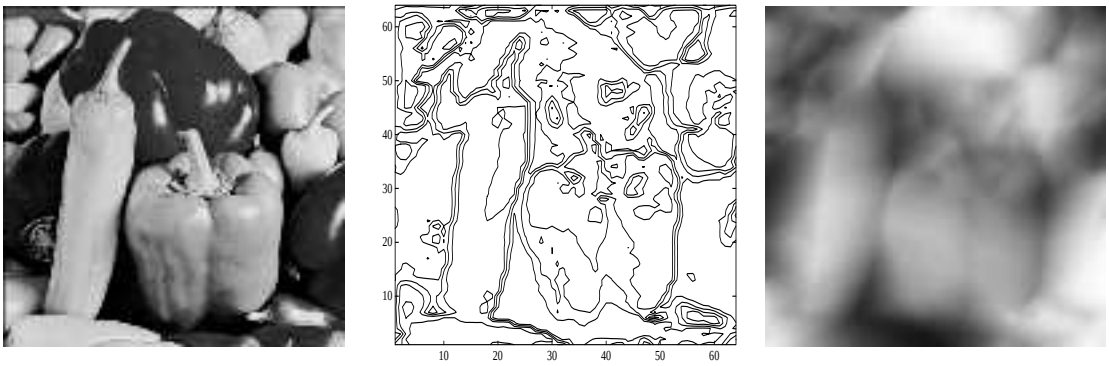

(a) (b) (c)

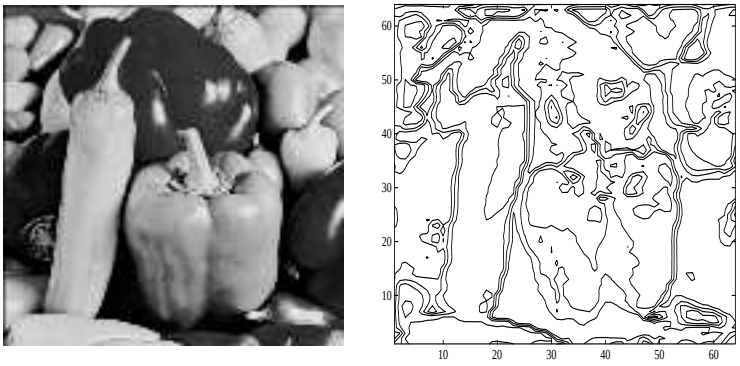

(d) (e)

Figure 11: SFS experiment on the peppers image. (a) The input image. (b) Contour map of the image in (a). (c) The height map obtained from SFS. (d) The image synthesized with the SFS result. (e) SFS reconstructed contour map.

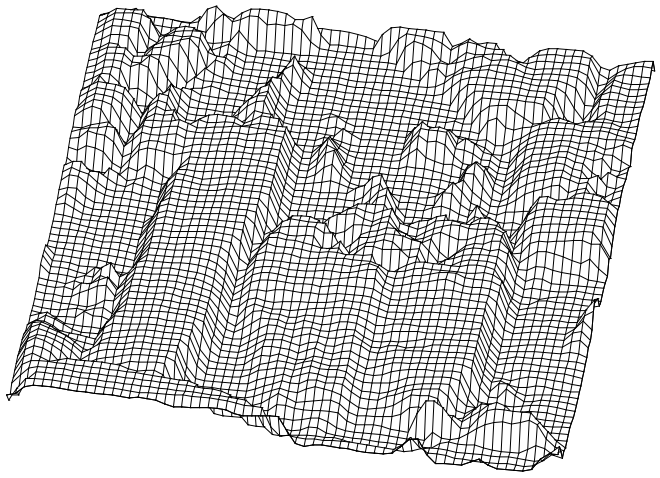

(f)

Figure 11: SFS experiment on the peppers image (contd.). (f) 3-D mesh plot of the height map of the reconstructed image.

References

[1] B.K.P. Horn and M.J. Brooks, *Shape From Shading*. Cambridge, MA:MIT Press, 1989.

[2] V.S. Ramachandran, "Perception of shape and shading," *Nature*, vol. 331, no. 14, pp. 163–166, Jan. 1988.

[3] B.K.P. Horn, "Shape from shading:A method for obtaining the shape of a smooth opaque object from one view," Ph.D. dissertation, Dept. of Electrical Engineering, MIT, Cambridge, MA, 1970.

[4] ____, "Height and gradient from shading," *Int. J. Comput. Vision*, vol. 5, no. 1, pp. 584–597, Aug. 1990.

[5] ____, "Hill shading and the reflectance map," *Proc. IEEE,* vol. 69, no. 1, pp. 448–455, Apr. 1982.

[6] M.J. Brooks and B.K.P. Horn, "Shape and source from shading," in *Proc. Int. Joint Conf. Comput. Artificial Intell.* (Los Angeles), pp. 932–936, Aug. 1985.

[7] C.H. Lee and A. Rosenfeld, "Improved methods of estimating shape from shading using the light source coordinate system," in B.K.P. Horn and M.J. Brooks, *Eds., Shape from Shading*. Cambridge, MA: MIT Press, pp. 323–569, 1989.

[8] T. Simchony, R. Chellappa, and M. Shao, "Direct analytic methods for solving Poisson equations in computer vision problems," *IEEE Trans. Pattern Anal. Machine Intell.,* vol. PAMI-12, no. 5, pp. 435–446, May 1990.

[9] K. Ikeuchi and B.K.P. Horn, "Numerical shape from shading and occluding boundaries," *Artificial Intell.,* vol. 17, pp. 141–184, Aug. 1981.

[10] B.K. Horn and M.J. Brooks, "The variantional approach to shape from shading," *Comput. Vision, Graphics, Image Processing,*, vol. 33, pp. 174–208, Nov. 1986.

[11] R.T. Frankot and R. Chellappa, "A method for enforcing integrability in shape from shading algorithms," *IEEE Trans. Pattern Anal. Machine Intell.,* vol. PAMI-10, no. 4, pp. 439–451, July 1988.

[12] M. Shao, T. Simchony, and R. Chellappa, "New Algorithms for reconstruction of a 3-D depth map from one or more images," in *Proc. Comput. Vision Pattern Recognition* (Ann Arbor, MI), pp. 513–528, June 1988.

[13] Q. Zheng and R. Chellappa, "Estimation of illuminant direction, albedo, and shape from shading," *IEEE Trans. Pattern Anal. Machine Intell.,* vol. PAMI-13, no. 7, pp. 680–702, July 1991.

[14] S. Peleg and G. Ron, "Nonlinear multiresolution: A shape-from-shading example," *IEEE Trans. Pattern Anal. Machine Intell.,* vol. PAMI-12, no. 12, pp. 1206–1210, 1990.